PAPER

Check for updates

Facile one-step synthesis and enhanced photocatalytic activity of a WC/ferroelectric nanocomposite†

Man Zhang,[a] Yaqiong Wang,[b] Jianguo Liu, [ID][c] Madasamy Thangamuthu,[d] Yajun Yue,[e] Zhongna Yan,[eg] Jingyu Feng, [ID][f] Dou Zhang, [ID][g] Hongtao Zhang,[h] Shaoliang Guan,[i] Maria-Magdalena Titirici, [ID][f] Isaac Abrahams, [ID][e] Junwang Tang, [ID][d] Zhen Zhang, [ID][j] Steve Dunn*[b] and Haixue Yan [ID] *[a]

The development of noble-metal-free co-catalysts is seen as a viable strategy for improving the performance of semiconductor photocatalysts. Although the photocatalytic efficiency of ferroelectrics is typically low, it can be enhanced through the incorporation of a co-catalyst into nanocomposites. Here, we demonstrate the influence of ferroelectricity on the decolorization of rhodamine B under simulated solar light using $RbBi_2Ti_2NbO_{10}$ and compared the performance with that of non-ferroelectric $RbBi_2Nb_5O_{16}$. The decolorization rate for $RbBi_2Ti_2NbO_{10}$ was 5 times greater than that of $RbBi_2Nb_5O_{16}$. This behaviour can be explained in terms of ferroelectric polarization, which drives the separation of charge carriers. The photocatalytic activity of $RbBi_2Ti_2NbO_{10}$ was further enhanced to over 30 times upon preparing a nanocomposite with tungsten carbide (WC) through high energy ball milling. This enhancement was attributed not only to the increased specific surface area, but also to the incorporated WC co-catalyst, which also serves as a source of plasmonic hot electrons and extends the photocatalytic activity into the visible light range. The $WC/RbBi_2Ti_2NbO_{10}$ nanocomposite shows interesting water oxidation properties and evolves O_2 with a rate of 68.5 μmol h^{-1} g^{-1} and a quantum yield of 3% at 420 nm. This work demonstrates a simple route for preparing WC containing nano-ferroelectric composites for solar energy conversion applications.

1. Introduction

The development of low cost photocatalyst materials with high photocatalytic efficiency which are also environmentally benign

[a]School of Engineering and Materials Science, Queen Mary University of London, Mile End Road, London E1 4NS, UK. E-mail: h.x.yan@qmul.ac.uk

[b]School of Engineering, London South Bank University, 103 Borough Road, London, SE1 0AA, UK. E-mail: dunns4@lsbu.ac.uk

[c]School of Environment, Tsinghua University, 1 Qinghuayuan, Beijing, 100084, China

[d]Department of Chemical Engineering, University College London, Torrington Place, London, WC1E 7JE, UK

[e]Department of Chemistry, Queen Mary University of London, Mile End Road, London E1 4NS, UK

[f]Department of Chemical Engineering, Imperial College London, South Kensington Campus, London SW7 2AZ, UK

[g]State Key Laboratory of Powder Metallurgy, Central South University, South Lushan Road, Changsha, 410083, China

[h]Department of Materials, Loughborough University, Leicestershire, LE11 3TU, UK

[i]School of Chemistry, Cardiff University, Main Building, Park Place, Cardiff, CF10 3AT, UK

[j]Division of Solid State Electronics, Department of Electrical Engineering, Uppsala University, Lagerhyddsvagen 1, Uppsala, Sweden

† Electronic supplementary information (ESI) available. See DOI: 10.1039/d1ta04131b

is viewed as a matter of global urgency.[1] In this respect, the direct use of natural solar energy through photocatalysts represents an important area of technology. When refined, the approach could be used to provide useful chemicals,[2] reduce CO_2 in the atmosphere[3] or produce fuels using narrow band-gap materials.[4] Despite abundant studies on semiconductors, including a variety of inorganic metal oxides (such as TiO_2, ZnO, WO_3 and SnO)[5–9] and sulfides (ZnS and CdS)[10–14] and the development of a variety of structures,[15] their photocatalytic efficiency is still far from satisfactory. A key challenge for efficiency improvement is suppressing the recombination of photo-induced charge carriers and prolonging their lifetime.[10,16–18] One important strategy to address this problem is to use ferroelectric materials. Their switchable spontaneous polarization produces internal electric fields,[19–22] resulting in the spatial separation of photo-induced electron–hole pairs.[23,24]

Morris *et al.*[25] tested the charge carrier lifetime in films of cubic (paraelectric) and tetragonal (ferroelectric) $BaTiO_3$ using transient absorption spectroscopy and found that the charge carrier lifetime in ferroelectric $BaTiO_3$ was four orders of magnitude longer than that in paraelectric $BaTiO_3$. A prolonged charge carrier lifetime is also reported in the Aurivillius ferroelectric, $Bi_{6-x}Sr_xTi_{3+x}Fe_{2-x}O_{18}$.[26] This clearly demonstrates that

the presence of internal fields can reduce the recombination of charge carriers, leading to enhanced photocatalytic efficiency. Moreover, the ferroelectric domains cause band bending of the electronic states and induce spatially selective reactivity for photochemical reactions, as demonstrated in perovskites, such as $BiFeO_3$,[27] $BaTiO_3$,[28] and $Pb(Zr_{0.3}Ti_{0.7})O_3$.[29] Among various ferroelectric photocatalysts with a perovskite-like structure, bismuth-containing niobates are reported as promising candidates,[30–32] due to the high energy of the Nb 4d conduction band[32] and the O 2p orbitals hybridized by Bi 6s in the valence band.[33,34] Moreover, depending on the Bi/Nb ratio, these compounds can adopt complex crystal structures, such as pyrochlore, layered perovskite or fluorite related structures, and thus exhibit different dielectric properties.[35] Although previous studies have reported the ferroelectricity of bismuth-containing niobates with layered perovskite structures, the effect of their polarization on photocatalysis has been barely studied.[36]

Loading a co-catalyst onto a ferroelectric material has been proved to be an effective strategy to further boost the photocatalytic efficiency.[37–39] The co-catalyst not only provides catalytic sites, but also suppresses the recombination of photoinduced charge carriers in the photocatalyst.[40,41] The most popular co-catalysts are noble metals, such as Au, Pt, Rh, and Ru. However, their high cost and scarcity hamper large-scale commercial applications, and thus the development of earth-abundant and inexpensive alternatives is essential. Both tungsten (W) and carbon (C) are earth-abundant, while tungsten carbide (WC) exhibits high electronic conductivity and has Pt-like d-band electronic density states.[42] Since Levy and Boudart's first report on WC in the catalysis of hydrogenolysis,[43] it has been intensively studied as an electrocatalyst support for methanol oxidation, oxygen reduction, nitrophenol oxidation and hydrogen evolution.[44,45] Hence, it is extremely desirable to prepare nanocomposites of ferroelectric photocatalyst particles with WC to enhance the photocatalytic activity. An intimate interfacial contact between WC and ferroelectric particles maximizes the reaction active sites and facilitates the charge transfer between the different phases. Different processing routes have been employed to produce WC particles,[46,47] such as direct carburization of tungsten powder, solid-state metathesis, reduction carburization,[48] mechanical grinding,[49] thermal pyrolysis of tungsten-containing organic acid,[47] polymeric precursor routes using metal alkoxides, hydrothermal methods,[50] *etc.* However, these processing routes are limited due to complicated apparatus and procedures, long processing times, high temperatures, and high-energy consumption.[51] Depending on the processing conditions, the obtained nanocomposites can have an inhomogeneous distribution of constituent phases, uncontrollable size, and weak interactions between the semiconductor and WC phases.[52] Thus, the efficient production of WC containing nanocomposites using low cost approaches remains a scientific and technological challenge.

Traditionally, the ball-milling method is used to prepare sub-micron sized particles, and high energy ball milling can be used to prepare nano-sized particles. Using the high energy ball milling approach, the ball milled material, for instance, the photocatalyst, could be coated with a secondary or foreign material which can be introduced from both the milling balls and milling jar. In this study, two Rb- and Bi-containing niobates, ferroelectric $RbBi_2Ti_2NbO_{10}$ (ref. 53) and non-ferroelectric $RbBi_2Nb_5O_{16}$ (ref. 54) materials, were prepared to investigate the impact of ferroelectric polarization on photocatalytic properties. To enhance the photocatalytic performance of ferroelectric $RbBi_2Ti_2NbO_{10}$, a WC co-catalyst was loaded onto the $RbBi_2Ti_2NbO_{10}$ nanopowder by a facile one-step high-energy ball milling processing technique.

The ferroelectric $RbBi_2Ti_2NbO_{10}$ has a larger bandgap (3.25 eV) with a lower specific surface area (7.72 m^2 g^{-1}) compared to the values (3.02 eV and 13.85 m^2 g^{-1}) of non-ferroelectric $RbBi_2Nb_5O_{16}$. However, the decolorization rate for $RbBi_2Ti_2NbO_{10}$ was 5 times greater than for $RbBi_2Nb_5O_{16}$. The prepared $WC/RbBi_2Ti_2NbO_{10}$ nanocomposite, produced using a facile route in only 40 min, showed over 30 times higher photocatalytic activity than the non-ferroelectric $RbBi_2Nb_5O_{16}$. Overall, this work demonstrates a novel approach to produce noble-metal-free co-catalyst loaded nanocomposites in an efficient and ultra-fast way for photocatalytic applications.

2. Results and discussion

Fig. 1a and b show the fitted room temperature X-ray diffraction (XRD) patterns of the calcined $RbBi_2Ti_2NbO_{10}$ and $RbBi_2Nb_5O_{16}$ powders. These two materials appear to be single phases with no detectable impurities. The atomic coordinates for $RbBi_2Ti_2NbO_{10}$ and $RbBi_2Nb_5O_{16}$ as reported by Kim *et al.*[53] and Ehlert *et al.*[54] were selected as the initial models for refinement. $RbBi_2Ti_2NbO_{10}$ is a 3-layer Dion–Jacobson phase, with orthorhombic symmetry and a polar space group of $Ima2$.[53] The peak splitting of (002) and (020) planes is related to the orthorhombic ferroelectric lattice distortion (Fig. 1a inset). $RbBi_2Nb_5O_{16}$ has a cubic defect pyrochlore structure with a non-polar space group of $Fd\bar{3}m$. Fig. 1c and d show the schematic crystal structures of
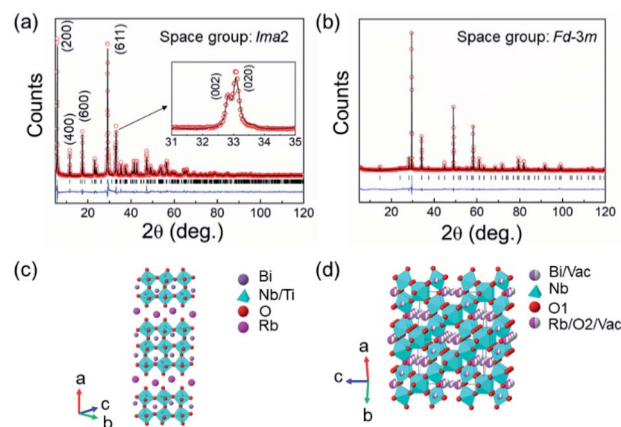

Fig. 1 Fitted X-ray diffraction patterns for (a) $RbBi_2Ti_2NbO_{10}$ and (b) $RbBi_2Nb_5O_{16}$. The observed and calculated profiles are represented by red open circles and a black solid line, respectively. The difference profile (blue line) and reflection positions (black markers) are also shown. Crystal structures of (c) $RbBi_2Ti_2NbO_{10}$ and (d) $RbBi_2Nb_5O_{16}$.

the studied compounds. $RbBi_2Ti_2NbO_{10}$ consists of 3 layers of corner sharing Ti/NbO_6 octahedra with Bi^{3+} cations in the A-sites. These perovskite blocks are separated by a layer of Rb^+ cations. On the other hand, $RbBi_2Nb_5O_{16}$ consists of a 3-dimensional network of corner sharing NbO_6 octahedra. While Bi^{3+} cations sit at the normal 8-coordinate pyrochlore sites (the actual coordination is lowered due to the partial occupancy of one of the oxygen sites), the Rb^+ cations are located in oxygen vacancies allowing these cations to adopt an octahedral geometry with oxygen. The fitting parameters and unit cell parameters for the samples are summarized in Table 1.

The relative densities of the sintered $RbBi_2Ti_2NbO_{10}$ and $RbBi_2Nb_5O_{16}$ ceramics were 92% and 95%. The morphological characterization of $RbBi_2Ti_2NbO_{10}$ ceramic shows plate-like grains (Fig. S1a†), whereas $RbBi_2Nb_5O_{16}$ ceramic was observed to have densely arranged grains in a polygonal pattern (Fig.- S1b†). The temperature dependence of the dielectric permittivity and loss of $RbBi_2Ti_2NbO_{10}$ ceramic is presented for the first time (Fig. 2a). A frequency independent peak is observed at around 506 °C in the dielectric permittivity plots, implying that $RbBi_2Ti_2NbO_{10}$ is ferroelectric with a Curie point (T_c) at this temperature. The loss peak appears a few degrees below T_c, which has been attributed to ferroelectric domain wall movement.[55] Although ferroelectric polarization–electric field loops have been reported,[53] there was no evidence to show domain switching in the loops. The published loops show a dominant contribution from conductivity and the highest polarization was less than $0.3\ \mu C\ cm^{-1}$. It is considered a requirement of ferroelectricity to have a measured switchable polarization loop. As such our measured loops are the first definitive evidence of ferroelectricity in the system.

The current–electric field (I–E) and displacement–electric field (D–E) loops of $RbBi_2Ti_2NbO_{10}$ were first measured at room temperature at a frequency of 20 Hz. At this temperature, ferroelectric domain switching was not observed due to a large coercive field. The measurement was then carried out at 100 °C at the same frequency to facilitate domain switching at a reduced coercive field, as shown in Fig. 2b. The current peaks associated with ferroelectric domain switching are clearly observed in the I–E loop.[56,57] Moreover, when the $RbBi_2Ti_2NbO_{10}$ ceramics were poled at 100 °C, a piezoelectric constant (d_{33}) value of $14.7 \pm 0.2\ pC\ N^{-1}$ was detected. All these dielectric,
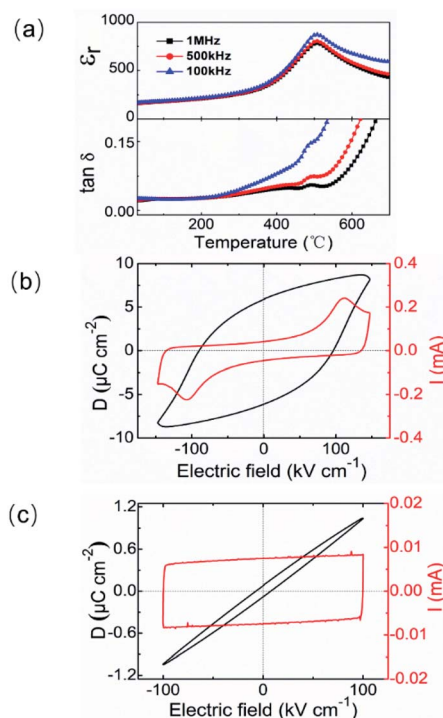

Fig. 2 (a) Temperature dependencies of dielectric permittivity (ε_r) and loss (tan δ) for $RbBi_2Ti_2NbO_{10}$; I–E and D–E loops of (b) $RbBi_2Ti_2NbO_{10}$ ceramic at 100 °C and (c) $RbBi_2Nb_5O_{16}$ ceramic at room temperature.

ferroelectric, and piezoelectric property results provide powerful evidence for the existence of ferroelectricity in $RbBi_2Ti_2NbO_{10}$. Similarly, I–E and D–E loops were tested for $RbBi_2Nb_5O_{16}$ at room temperature and 20 Hz (Fig. 2c). In contrast to $RbBi_2Ti_2NbO_{10}$, no current peaks were observed in the I–E loop of $RbBi_2Nb_5O_{16}$ ceramic, suggesting that this material has linear dielectric behaviour.[56,57] This is consistent with its non-polar structure.

The as-calcined $RbBi_2Ti_2NbO_{10}$ and $RbBi_2Nb_5O_{16}$ powders were first milled in nylon milling jars at 180 rpm for 24 h to obtain sub-micron sized powders (Fig. S2†). The sub-micron sized $RbBi_2Ti_2NbO_{10}$ powder is ferroelectric in nature, as confirmed by the PFM images shown in Fig. S3.† The specific surface areas of the sub-micron sized $RbBi_2Ti_2NbO_{10}$ and $RbBi_2Nb_5O_{16}$ powders were 7.72 and $13.85\ m^2\ g^{-1}$ (Table 2). The light absorption properties of both powders were characterized by UV-Vis spectroscopy (Fig. 3a). It is assumed that $RbBi_2Ti_2NbO_{10}$ and $RbBi_2Nb_5O_{16}$ are direct band gap materials, based on an analogy with the 2-layer Dion–Jacobson phase $CsBi_{1-x}Eu_xNb_2O_7$.[58] The band gaps (E_g) of $RbBi_2Ti_2NbO_{10}$ and

Table 1 Crystal and refinement parameters for $RbBi_2Ti_2NbO_{10}$ and $RbBi_2Nb_5O_{16}$

Composition	Crystal parameters	Refinement parameters
$RbBi_2Ti_2NbO_{10}$	Orthorhombic (*Ima*2)	$\chi^2 = 3.92$
	$a = 30.5499\ (1)$ Å	$R_{wp} = 0.0987$
	$b = 5.4255\ (3)$ Å	$R_p = 0.072$
	$c = 5.4656\ (3)$ Å	$R_{ex} = 0.0502$
	$V = 905.9\ (1)$ Å^3	$R_{F2} = 0.1292$
$RbBi_2Nb_5O_{16}$	Cubic ($Fd\bar{3}m$)	$\chi^2 = 4.286$
	$a = 10.5268\ (1)$ Å	$R_{wp} = 0.1032$
	$V = 1166.52\ (1)$ Å^3	$R_p = 0.08$
		$R_{ex} = 0.0500$
		$R_{F2} = 0.1003$

Table 2 Properties of sub-micron sized $RbBi_2Ti_2NbO_{10}$ and $RbBi_2Nb_5O_{16}$ powders

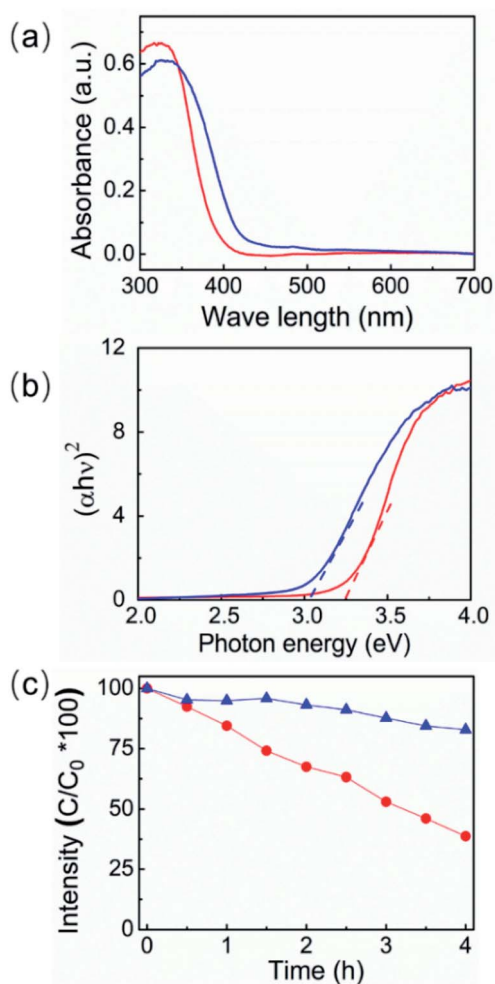| Catalyst	$RbBi_2Ti_2NbO_{10}$	$RbBi_2Nb_5O_{16}$
Band gap (eV)	3.25	3.02
Specific surface area ($m^2\ g^{-1}$)	7.72	13.85
Decolorization rate (min^{-1})	3.8×10^{-3}	7.4×10^{-4}

Fig. 3 Light absorption and photocatalytic property characterisation of sub-micron sized $RbBi_2Ti_2NbO_{10}$ (red curves) and $RbBi_2Nb_5O_{16}$ powders (blue curves): (a) UV-Vis absorption spectra; (b) illustration of $(\alpha h\gamma)^2$ versus photon energy (the optical bandgaps can be determined by the extrapolation of the linear portion); (c) photodegradation efficiencies of RhB as a function of irradiation time under simulated sunlight, where the lines serve as a guide to the eye.

$RbBi_2Nb_5O_{16}$, which were calculated by using the Tauc equation,[59] are 3.25 eV and 3.02 eV (Fig. 3b).

The photocatalytic activity of the $RbBi_2Ti_2NbO_{10}$ and $RbBi_2Nb_5O_{16}$ powders was tested through the photodecomposition of RhB and the degradation profiles are shown in Fig. 3c. It can be seen that the ferroelectric $RbBi_2Ti_2NbO_{10}$ degrades about 60% of the dye within 4 h, whereas the non-ferroelectric $RbBi_2Nb_5O_{16}$ degrades about 12% over the same time period. The decolorization rate was calculated according to the following equation:

$$\ln\left(\frac{C_0}{C_t}\right) = k_{obs}t$$

where C_0 and C_t are the concentration of RhB at times 0 and t, respectively, and k_{obs} is the observed pseudo-first-order reaction rate constant.[60] The ratio $C_0/C_t = A_0/A_t$ corresponds to the measured absorbances. As shown in Table 2, the decolorization

rate constants of sub-micron sized $RbBi_2Ti_2NbO_{10}$ and $RbBi_2Nb_5O_{16}$ powders are 3.8×10^{-3} and 7.4×10^{-4} min^{-1}, respectively. Although the $RbBi_2Ti_2NbO_{10}$ powder has a slightly larger bandgap and a smaller specific surface area, it shows a 5 times higher decolorization rate compared to $RbBi_2Nb_5O_{16}$. The higher photocatalytic activity shown by $RbBi_2Ti_2NbO_{10}$ can be attributed to its ferroelectric nature[60,61] and the internal field generated by spontaneous polarization which promotes the separation of charge carriers and reduces their recombination. It should be noted that the orthorhombic phase of $RbBi_2Ti_2NbO_{10}$ provides an additional opportunity to support charge separation by anisotropic surface potentials in the layered structure.[62]

It was reported by Levy and Boudart[43] that WC has platinum-like behaviour and facilitates redox reactions. In order to study the effect of WC on the photocatalytic activity of the $RbBi_2Ti_2NbO_{10}$ material, the calcined $RbBi_2Ti_2NbO_{10}$ powder was ball milled at a higher rotation speed of 600 rpm for 40 min using the same ZrO_2 milling balls. For this control experiment, two different types of milling jars, made of ZrO_2 and WC, were used in an attempt to introduce WC into the surface of $RbBi_2Ti_2NbO_{10}$ powder. The ZrO_2 jar was used for comparison. The XRD patterns of the ball milled powders are shown in Fig. S4.† Diffraction peaks for both $RbBi_2Ti_2NbO_{10}$ and ZrO_2 are present, which indicates the introduction of ZrO_2 from the milling balls into the $RbBi_2Ti_2NbO_{10}$ powder due to intense collision between the milling balls/jar and the ceramic powder. The photocatalytic degradation of RhB under simulated solar light irradiation using these two composite powders was studied and the results are shown in Fig. S5† and Table 3. Although the composite powder ball milled in the ZrO_2 jar has a larger specific surface area (Table 3), a lower photodegradation rate was observed. The composite prepared in the WC jar shows almost 100% dye degradation within 3 h, whereas the composite prepared in the ZrO_2 jar shows about 90% dye degradation in 4 h. Considering that the composite powders prepared in the WC jar and ZrO_2 jar have similar specific surface areas, the enhanced photocatalytic activity of the composite powder made in the WC jar is attributed to the contribution from WC. The control experimental results indicated a route to optimize the preparation conditions for further enhancing the photocatalytic activity of $RbBi_2Ti_2NbO_{10}$. As such, the calcined $RbBi_2Ti_2NbO_{10}$ powder was ball milled in a WC jar under different rotation speeds and durations, details of which are listed in Table S1.† The XRD patterns of the powder are shown in Fig. S6.† With increasing rotation speed and ball milling time, the diffraction peaks of the powders became broader, indicative of the decreasing particle size of the powder. The

Table 3 Photocatalytic properties of $RbBi_2Ti_2NbO_{10}$ nanopowders prepared using different milling jars at 600 rpm for 40 min

Jar type	Specific surface area (m^2 g^{-1})	Degradation rate (min^{-1})
WC	19.47	0.016
ZrO_2	21.99	0.009

photodegradation of RhB was carried out to characterize the photocatalytic behaviour of the obtained powders (Fig. S7†). The ball milling parameters, specific surface areas, and photo-degradation rate of RhB of the obtained nanocomposites are shown in Table S1.† For an easier comparison, the powder ball milled in a WC jar at 600 rpm for 40 min (Table 3) is also shown in Table S1.† It is clear that at 600 rpm, the degradation rate of RhB firstly increases and then decreases with increasing ball-milling time. The initial increase in the photodegradation rate is attributed to the increased specific surface area; however, further reduction in the particle size reduced the photocatalytic activity. This may be due to a blocking effect associated with the ZrO_2 from the milling balls and/or decreased polarization in powders with a smaller particle size, which is discussed below. The best photocatalytic activity was observed with a ball milling speed of 800 rpm and a 40 min milling time.

The role of WC in the nanocomposite prepared under these conditions was studied in detail. The obtained nanocomposite consisted of three nanocrystalline phases ($RbBi_2Ti_2NbO_{10}$, ZrO_2, and WC), but as discussed below, ZrO_2 gives no contribution to the photocatalytic response under the irradiation conditions used here. Hence, we use the term "WC/$RbBi_2Ti_2$-NbO_{10} nanocomposite" for simplicity. Compared with the sub-micron sized powder, the width of the $RbBi_2Ti_2NbO_{10}$ diffraction peaks in the nanocomposite is broader, indicating that the average crystallite size is smaller. The introduction of WC from the WC milling jar into $RbBi_2Ti_2NbO_{10}$ could not be confirmed by XRD due to the lack of detectable diffraction peaks (Fig. S6†). Fig. 4a shows detail of the (002) and (020) peaks in the XRD patterns of sub-micron sized $RbBi_2Ti_2NbO_{10}$ and WC/$RbBi_2$-Ti_2NbO_{10} nanocomposites. These peaks were modelled using a simple pseudo-Voigt peak shape. The peak splitting is clearly discernible in the sub-micron sized sample and less clear in the nanocomposite due to the peak broadening. Nevertheless, asymmetry in the distribution is obvious and the two peaks were successfully fitted indicating that the ferroelectric distortion is maintained, albeit slightly reduced in magnitude in the nano-composite. The spontaneous polarization P_s in $RbBi_2Ti_2NbO_{10}$ depends on the extent of orthorhombic distortion, which can be quantified from the orthorhombicity, $(c - b)/b$, where b and c are lattice parameters.

According to the fitting results, the orthorhombicity values for sub-micron sized $RbBi_2Ti_2NbO_{10}$ and WC/$RbBi_2Ti_2NbO_{10}$ nanocomposites are 0.74% and 0.46%, respectively. The smaller orthorhombicity value in the WC/$RbBi_2Ti_2NbO_{10}$ nano-composite suggests that the P_s is reduced compared to that in the sub-micron sized powder.[24,63] This can be attributed to the size effect on the ferroelectric domain structure.[64,65] When the sizes of ferroelectric particles/grains are in the micrometre range, domain walls are generated to minimize the internal stresses induced by phase transition from the paraelectric to the ferroelectric phase at the Curie point. In this case, P_s and orthorhombicity are insensitive to changes in the particle/grain size. When the particle/grain size of ferroelectric powders is reduced to the nanometre range, the orthorhombic distortion reduces. Therefore, there is no necessity for domain wall
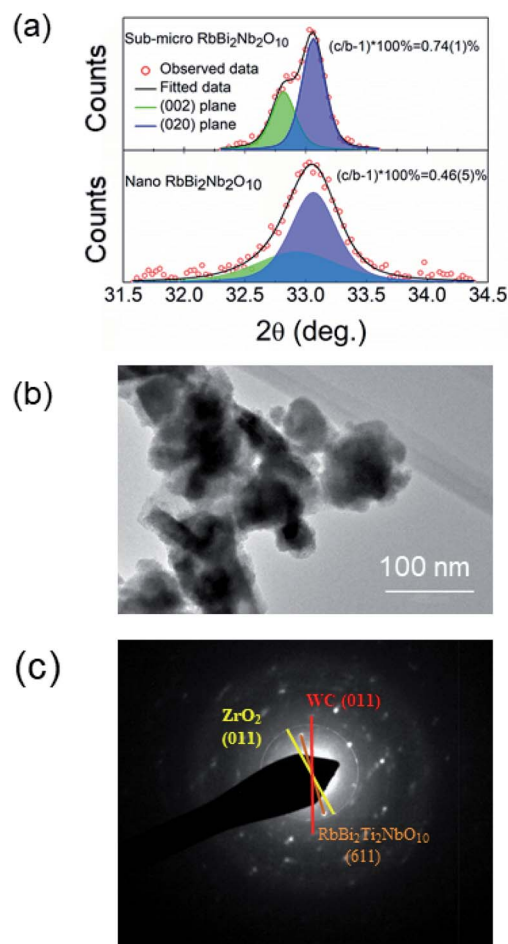

Fig. 4 (a) Details of the X-ray diffraction patterns for sub-micron $RbBi_2Ti_2NbO_{10}$ and WC/$RbBi_2Ti_2NbO_{10}$ nanocomposites showing pseudo-Voigt fit to (020) and (002) diffraction peaks; (b) TEM image of the WC/$RbBi_2Ti_2NbO_{10}$ nanocomposite and (c) corresponding SAED pattern.

formation to minimize the internal stresses, which are already reduced as the P_s is decreased.[66,67]

Fig. 4b shows a TEM image of the WC/$RbBi_2Ti_2NbO_{10}$ nanocomposite. Granular powders with an average particle size of *ca.* 80 nm can be observed. The specific surface area deter-mined by the BET method was 19.77 m^2 g^{-1} (Table S1†). The selected area electron diffraction (SAED) image (Fig. 4c) shows the diffraction spots from the (611) plane of $RbBi_2Ti_2NbO_{10}$. Although ZrO_2 and WC particles were not noticeable from the TEM images, the diffraction spots from the (011) plane of WC[68] and the (011) plane of ZrO_2 (ref. 69) are visible. This confirms the existence of WC and ZrO_2 nanoparticles within the nanocomposite.

UV absorption (Fig. 5a) and valence band X-ray photoelec-tron spectroscopy (XPS) (Fig. S9†) were used to determine the band structure of the WC/$RbBi_2Ti_2NbO_{10}$ nanocomposite. ZrO_2 was expected to have no contribution to the photocatalytic response under simulated solar irradiation with a wavelength longer than 280 nm due to its large band gap ($\sim$5.7 eV)[70] and therefore the discussion below is focused on the
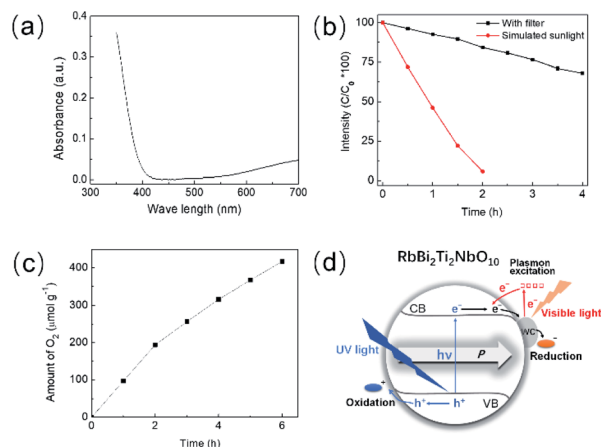
Fig. 5 (a) Light absorption and photocatalytic property characterisation of the WC/RbBi$_2$Ti$_2$NbO$_{10}$ nanocomposite; (b) degradation of RhB with the WC/RbBi$_2$Ti$_2$NbO$_{10}$ nanocomposite under simulated sunlight (red) and visible light (black) (lines serve as a guide to the eye); (c) O$_2$ evolution from water (pH 7.0) using 30 mg of RbBi$_2$Ti$_2$NbO$_{10}$ containing 10 mM AgNO$_3$, as an electron scavenger under full arc conditions for 6 h; (d) schematic of the redox reaction on the surface of a WC/RbBi$_2$Ti$_2$NbO$_{10}$ nanocomposite particle.

photocatalytically active components. The WC/RbBi$_2$Ti$_2$NbO$_{10}$ nanocomposite not only showed strong absorption at wavelengths shorter than 400 nm, but also showed weak but broad absorption in the longer wavelength range (Fig. 5a), which indicates the absorption of visible light. The band gap for the WC/RbBi$_2$Ti$_2$NbO$_{10}$ nanocomposite was calculated to be 3.25 eV (Fig. S8†), confirming that the powder particle size reduction in RbBi$_2$Ti$_2$NbO$_{10}$ does not alter the band gap value. The valence band XPS spectrum in Fig. S9a† confirms the metal like behaviour of WC.[71] By comparing Fig. S9a and b,† it is concluded that the Fermi level of WC is lower than the conduction band level of RbBi$_2$Ti$_2$NbO$_{10}$ (Fig. S9c†). Morphological characterization via TEM reveals that the WC nanoparticles were homogeneously distributed within the WC/RbBi$_2$Ti$_2$NbO$_{10}$ nanocomposite (Fig. S10†).

The photodegradation of RhB using the WC/RbBi$_2$Ti$_2$NbO$_{10}$ nanocomposite under simulated sun light and visible light irradiations was investigated, and the results are shown in Fig. 5b. Almost 100% of the RhB dye was degraded at a rate of 2.3×10^{-2} min^{-1} (Table 4) within 2 hours while irradiated using simulated sunlight, which is 6 times higher than that with sub-micron sized RbBi$_2$Ti$_2$NbO$_{10}$ and over 30 times higher than that with non-ferroelectric RbBi$_2$Nb$_5$O$_{16}$. As discussed above, the driving force for charge carrier separation in RbBi$_2$Ti$_2$NbO$_{10}$ powders would reduce with decreasing particle size down to the nanoscale owing to the reduced orthorhombicity and P_s. The size reduction of RbBi$_2$Ti$_2$NbO$_{10}$ is expected to compromise the photocatalytic activity to some extent. However, the positive contribution from the greater specific surface area of the ferroelectric nanoparticles, the efficient charge separation and transport by the WC incorporation and possibly severe plastic deformation caused by high-speed ball milling[72] overwhelm the decreased ferroelectric contribution in the WC/RbBi$_2$Ti$_2$NbO$_{10}$

nanocomposite and contribute to its enhanced photocatalytic activity.

To prove the above claim and determine the role of WC, we further characterized the nanocomposite of WC/RbBi$_2$Ti$_2$-NbO$_{10}$. Under visible light irradiation, the WC/RbBi$_2$Ti$_2$NbO$_{10}$ nanocomposite photo-catalytically degrades 32% of RhB within 4 h (Fig. 5b), whereas sub-micron sized RbBi$_2$Ti$_2$NbO$_{10}$ shows no photocatalytic activity. These results suggest that the observed photocatalytic activity under visible light is originated from the WC. It is worth noting that the nanoparticles of WC show surface plasmon properties.[73] Various plasmonic properties such as plasmonic scattering, near-field coupling, and hot electrons have been reported for photocatalysis.[74,75] However, in the present case, we expect that the plasmonic hot electrons generated from the WC nanoparticles may transfer to the RhB molecule directly to degrade or enter into the conduction band (CB) of RbBi$_2$Ti$_2$NbO$_{10}$, which later reduces the RhB molecule. The broad visible absorption peak observed for WC/RbBi$_2$Ti$_2$-NbO$_{10}$ (Fig. 5a), in the range of 500 nm to 700 nm, is attributed to the plasmonic WC particles with various sizes.[73,76]

To verify the stability of the material, 3 cycles of RhB degradation were performed under simulated sunlight (Fig. S11†) and no significant changes were observed, suggesting that the WC/RbBi$_2$Ti$_2$NbO$_{10}$ nanocomposite is stable enough under the present experimental conditions.

The photocatalytic water oxidation activity of the WC/RbBi$_2$Ti$_2$NbO$_{10}$ nanocomposite was studied in the presence of Ag as an electron scavenger under full arc (similar to solar light) conditions. A significant O$_2$ evolution was observed at pH 7.0 with an average gas evolution rate of 68.5 μmol h^{-1} g^{-1} (Fig. 5c). In the absence of a photocatalyst as well as in the absence of an electron scavenger, no O$_2$ evolution was observed, in addition to no activity under dark conditions. It can be seen from Fig. 5c that the rate of O$_2$ evolution was higher during the early hours of the reaction, which may be due to the prearrangements of the photocatalytic system to produce O$_2$ with a steady rate after 3 h of irradiation. It exhibits an apparent quantum yield (AQY) of 3% at 420 nm. This value is significant because the photocatalytic water oxidation using the present ferroelectric material is relatively new and competitive to conventional water oxidation photocatalysis. These results are encouraging for the use of such ferroelectric materials in solar-driven photocatalysis.

Fig. 5d schematically describes the redox reaction on the surface of the WC/RbBi$_2$Ti$_2$NbO$_{10}$ nanocomposite. Under UV light, electrons produced from RbBi$_2$Ti$_2$NbO$_{10}$ participate in the degradation reactions with WC acting as a cocatalyst to enhance charge carrier separation and transfer. In addition, it is expected that the Fermi energy of WC with Pt-like electronic features would be lower than the conduction band of RbBi$_2$-Ti$_2$NbO$_{10}$.[76] The plasmonic hot electrons generated in the WC nanoparticles contribute to photodegradation in the visible light range. The approach used here for enhanced semiconductor visible light photocatalysis using nano-sized WC could be applied to a broad range of semiconductor/co-catalyst materials for high performance photocatalysis.

Although the ferroelectric RbBi$_2$Ti$_2$NbO$_{10}$ material has a larger band gap, it can be used for photocatalytic applications

Table 4   Comparison of the photocatalytic performance of ferroelectric photocatalysts

Photocatalyst	Band gap/eV	Catalytic conditions	Catalytic application	Catalytic activity	Ref.
$KNbO_3$ nanowire	3.25	UV light	RhB degradation	$K_{obs} = 4.2 \times 10^{-3}$ min^{-1}	77
$Au/KNbO_3$ nanowire	3.81	UV light	RhB degradation	$K_{obs} = 1.6 \times 10^{-2}$ min^{-1}	78
Bi_2WO_6 nanoparticle	2.9	Visible light	RhB degradation	$K_{obs} = 1.2 \times 10^{-2}$ min^{-1}	79
Ag/Bi_2WO_6 nanoparticle	2.9	Visible light	RhB degradation	$K_{obs} = 3.3 \times 10^{-2}$ min^{-1}	79
$Ag/Bi_4Ti_3O_{12}$	2.9	UV light	RhB degradation	$K_{obs} = 1.3 \times 10^{-2}$ min^{-1}	80
$Pt/Bi_4Ti_3O_{12}$	2.9	UV light	RhB degradation	$K_{obs} = 1.5 \times 10^{-2}$ min^{-1}	80
$Ag/BaBi_4Ti_4O_{15}$	3.2	Simulated solar light	RhB degradation	Complete within 3.5 h	81
$Ag/BaBi_2Nb_2O_9$	3.2	Simulated solar light	RhB degradation	Complete within 3 h	82
$Ag/Ca_2Bi_4Ti_5O_{18}$	3.2	Simulated solar light	RhB degradation	50% degradation within 4 h	83
$Ag/RbBiNb_2O_7$ nanosheet	3.45	UV-light	RhB degradation	$K_{obs} = 8.7 \times 10^{-3}$ min^{-1}	84
$Ag/Ba_{0.8}Sr_{0.2}TiO_3$	3.24	Simulated solar light	RhB degradation	$K_{obs} = 0.18$ min^{-1}	67
$WC/RbBi_2Ti_2NbO_{10}$	3.25	Simulated solar light	RhB degradation	$K_{obs} = 2.3 \times 10^{-2}$ min^{-1}	This work
$Pt/LiNbO_3$ nanowire	—	UV-light	O_2 evolution	19 μmol g^{-1} h^{-1}	85
$WC/RbBi_2Ti_2NbO_{10}$	3.25	Simulated solar light	O_2 evolution	68.5 μmol g^{-1} h^{-1}	This work

using the present facile one step high speed ball milling method. Table 4 lists the photocatalytic properties of ferroelectric photocatalysts. The photodegradation rate of RhB and the O_2 production rate are much higher than those of reported ferroelectric photocatalysts.

3.   Experimental

$RbBi_2Ti_2NbO_{10}$ and $RbBi_2Nb_5O_{16}$ powders were synthesized by a conventional solid-state reaction. Rb_2CO_3 (99.8%), Bi_2O_3 (99.9%), Nb_2O_5 (99.5%), and TiO_2 (99%) powders were mixed in a stoichiometric ratio (with 4 wt% excess of Rb_2CO_3) by planetary ball milling (Fritsch Pulverisette 6) in ethanol using nylon milling jars and ZrO_2 balls with a diameter of 10 mm for 4 h at a speed of 180 rpm. The resulting slurry was dried overnight at 80 °C. The dried powders were calcined at 920 °C for 4 h for $RbBi_2Ti_2NbO_{10}$ and 980 °C for 4 h for $RbBi_2Nb_5O_{16}$ followed by dry grinding using an agate mortar and pestle.

The calcination and grinding processes were carried out three times. Calcination at high temperature resulted in an agglomeration of powders. In order to reduce the agglomerate size and to facilitate subsequent sintering, the calcined powders were re-milled by planetary ball milling in ethanol for 4 h. The resulting powders were pressed into cylindrical discs of 10 mm diameter and ca. 2 mm thickness, with poly (ethylene glycol) (PEG) as a binder, at 200 MPa. The pressed pellets were sintered at 950 °C for $RbBi_2Ti_2NbO_{10}$ and 1050 °C for $RbBi_2Nb_5O_{16}$ for 2 h in air. The surfaces of the sintered ceramics were polished and coated with Pt paste for dielectric measurements and Ag paste for ferroelectric and piezoelectric measurements.

For photocatalytic studies, the calcined $RbBi_2Ti_2NbO_{10}$ and $RbBi_2Nb_5O_{16}$ powders were milled in ethanol using ZrO_2 milling balls with a diameter of 10 mm in nylon milling jars at a rotation speed of 180 rpm for 24 h, producing sub-micron sized powders. In order to investigate the effect of WC on the photocatalytic performance of $RbBi_2Ti_2NbO_{10}$, control experiments, which were designed to load the $RbBi_2Ti_2NbO_{10}$ powder with WC using high energy ball milling, were carried out. The high energy ball milling machine used is a Fritsch Premium line

P7 planetary ball milling machine. The difference in the two parallel control experiments is the milling jars, with one experiment using a WC jar and the other using a ZrO_2 jar for comparison. The same amount of calcined $RbBi_2Ti_2NbO_{10}$ powder was loaded into the milling jar and ball milled at a speed of 600 rpm for 40 min. The milling medium is DI water and the milling balls were 1 mm ZrO_2 balls. Although attempts were made to use WC milling balls in the WC jar to get a better composition, they were not successful due to the limited commercial availability of small diameter WC milling balls (high rotation speed and hard milling balls with a small diameter are required for the production of nanopowders via planetary ball milling[86]). Moreover, to optimize the properties of $WC/RbBi_2Ti_2NbO_{10}$ composite powder, the $RbBi_2Ti_2NbO_{10}$ powder was high energy ball milled in a WC jar for different durations (20 min and 120 min) and different rotation speeds (800 rpm).

Room temperature X-ray powder diffraction measurements were performed on a PANalytical X'Pert Pro diffractometer using Ni filtered Cu-Kα radiation ($\lambda = 1.5418$ Å). Data were collected in flat plate Bragg–Brentano geometry over the 2θ range of 5 to 120° in steps of 0.033°, with a count time of 200 s per step. Structure refinement was carried out by Rietveld analysis using the GSAS suite of programs.[87] The morphologies and microstructures of the samples were observed using scanning electron microscopy (FEI Inspect-F) and transmission electron microscopy [TEM, FEI Titan Themis (200 kV)], coupled with energy dispersive X-ray spectroscopy (EDX). Piezoresponse Force Microscopy (PFM) (NT-MDT, Ntegra systems, Russia) was used to characterize the domain structure. The specific surface area of the powders was determined using the Brunauer–Emmett–Teller (BET) (Gemini VII) method. The temperature dependencies of dielectric permittivity and loss were measured using an LCR meter (Agilent Technologies Ltd, 4284A, Kobe, Hyogo, Japan) connected to a furnace. The current–electric field (I–E) and displacement–electric field (D–E) loops were measured at selected temperatures using a ferroelectric hysteresis measurement tester (NPL, UK) at 20 Hz. A triangular voltage waveform was used. For piezoelectric measurements, ceramic

samples were immersed in a silicone oil bath and poled under a DC field of 130 kV cm^{-1} at 100 °C. The piezoelectric coefficient, d_{33}, was measured on a quasi-static d_{33} meter (CAS, ZJ-3B) at room temperature.

The band structures of WC and $RbBi_2Ti_2NbO_{10}$ were measured using valence band X-ray photoelectron spectroscopy (Nexsa, XPS system). The photocatalytic activity of the samples was evaluated by photodegradation of Rhodamine B (RhB) under simulated sunlight with wavelengths longer than 280 nm and visible light using an AM 1.5 filter. 150 mg of catalyst was added to 50 ml of aqueous RhB solution (10 ppm). The suspension was stirred continuously in the dark for 0.5 h before it was exposed to a solar simulator (Newport, class ABB). Under irradiation, 2 ml of solution was collected at intervals of 30 min. The ceramic particles were removed from the solution using a centrifuge before testing the change in the concentration of RhB by recording the absorbance at 554 nm using a UV-vis spectrophotometer. Recyclability experiments were carried out to test the stability of the $WC/RbBi_2Ti_2NbO_{10}$ nanocomposite. The quantity of the photocatalyst and RhB solution used was the same as that in previous photodegradation experiments. After 1.5 hours of the first photocatalytic test, the $WC/RbBi_2$-Ti_2NbO_{10} nanocomposite was washed and centrifuged three times for a second 1.5 hour cycle. This procedure was repeated a third time before being centrifuged and measuring the light absorbance.

Photocatalytic water splitting was carried out in a custom-made glass batch reactor with a quartz top window. 30 mg of the photocatalyst was dispersed in 70 ml of DI water containing 10 mM $AgNO_3$ using ultrasonication for 15 min. The reactor was sealed and purged with high purity argon gas for 1 h to remove the air/dissolved oxygen in the solution and headspace. The reactor was irradiated using a 300 W Xe lamp (Newport, USA). The reactor was placed in a water bath during irradiation to eliminate the influence of heat. The production of O_2 gas was quantified at regular intervals using a gas chromatograph (Varian 430-GC, TCD, and argon carrier gas) equipped with a molecular 5A column using Ar as the carrier gas. The apparent quantum yield (AQY) was determined by performing photocatalytic experiments using a 420 nm bandpass filter ($\lambda \pm 10$ nm at 10% of peak height, Comar Optics). The AQY was calculated using the following equation:

$$AQY\ (\%) = \frac{\alpha \times \text{amount of gas molecules evolved}}{\text{total number of incident photons}} \times 100\%$$

where $\alpha = 4$ for O_2 evolution.

4. Conclusions

In summary, we have successfully demonstrated a ferroelectric material, $RbBi_2Ti_2NbO_{10}$, for enhancing photocatalytic RhB degradation compared to non-ferroelectric $RbBi_2Nb_5O_{16}$. The observed higher activity is due to the effective charge carrier separation by the ferroelectric polarization induced internal field. Furthermore, the photocatalytic activity of $RbBi_2Ti_2NbO_{10}$ is increased significantly by incorporating WC, which also extended the activity to the visible range. The WC/

$RbBi_2Ti_2NbO_{10}$ nanocomposite shows a 6 times higher RhB degradation rate under simulated solar light than the sub-micron sized $RbBi_2Ti_2NbO_{10}$. This is attributed to the greater specific surface area, and the better charge carrier separation by the WC co-catalyst. The visible light photocatalytic activity of the $WC/RbBi_2Ti_2NbO_{10}$ nanocomposite is due to plasmonic hot electron generation from WC. More importantly, the present nanocomposite shows water oxidation activity suggesting that it can be used for solar fuel synthesis applications. Our promising results indicate the feasibility to use the earth abundant WC as a competitive co-catalyst to replace expensive noble metals. The novel approach for the incorporation of WC into semiconductor materials is a facile and low-cost way of producing noble-metal-free photocatalyst composites, and the strategy could be readily adapted to other classes of materials for a variety of applications.

Author contributions

Conflicts of interest

The authors declare no competing interests.

Acknowledgements

Notes and references

1 H. Tong, S. Ouyang, Y. Bi, N. Umezawa, M. Oshikiri and J. Ye, *Adv. Mater.*, 2012, **24**, 229–251.

2 C. Y. Toe, C. Tsounis, J. Zhang, H. Masood, D. Gunawan, J. Scott and R. Amal, *Energy Environ. Sci.*, 2021, **14**, 1140–1175.

3 S. C. Shit, I. Shown, R. Paul, K. H. Chen, J. Mondal and L. C. Chen, *Nanoscale*, 2020, **12**, 23301–23332.

4 J. Zheng, H. Zhou, Y. Zou, R. Wang, Y. Lyu, S. P. Jiang and S. Wang, *Energy Environ. Sci.*, 2019, **12**, 2345–2374.

5 C. Shifu, C. Lei, G. Shen and C. Gengyu, *Mater. Chem. Phys.*, 2006, **98**, 116–120.

6 R. Asahi, T. Morikawa, T. Ohwaki, K. Aoki and Y. Taga, *Science*, 2001, **293**, 269–271.

7 P. M. Rao, L. Cai, C. Liu, I. S. Cho, C. H. Lee, J. M. Weisse, P. Yang and X. Zheng, *Nano Lett.*, 2014, **14**, 1099–1105.

8 Q. Wu, F. Huang, M. Zhao, J. Xu, J. Zhou and Y. Wang, *Nano Energy*, 2016, **24**, 63–71.

9 S. Sun, X. Yu, Q. Yang, Z. Yang and S. Liang, *Nanoscale Adv.*, 2019, **1**, 34–63.

10 R. Macquart, B. J. Kennedy, T. Kamiyama and F. Izumi, *J. Phys. Condens. Matter.*, 2004, **16**, 5443.

11 Z. Xie, X. Liu, W. Wang, X. Wang, C. Liu, Q. Xie, Z. Li and Z. Zhang, *Nano Energy*, 2015, **11**, 400–408.

12 Q. Sun, N. Wang, J. Yu and J. C. Yu, *Adv. Mater.*, 2018, **30**, 1–7.

13 Z. Zhang, Q. Qian, B. Li and K. J. Chen, *ACS Appl. Mater. Interfaces*, 2018, **10**, 17419–17426.

14 L. Cheng, Q. Xiang, Y. Liao and H. Zhang, *Energy Environ. Sci.*, 2018, **11**, 1362–1391.

15 X. Li, J. Yu and M. Jaroniec, *Chem. Soc. Rev.*, 2016, **45**, 2603–2636.

16 J. Li, L. Cai, J. Shang, Y. Yu and L. Zhang, *Adv. Mater.*, 2016, **28**, 4059–4064.

17 H. Lei, M. Wu, Y. Liu, F. Mo, J. Chen, S. Ji, Y. Zou and X. Dong, *Chinese Chem. Lett.*, 2021, **32**, 2317–2321.

18 M. Wang, B. Wang, F. Huang and Z. Lin, *Angew. Chem., Int. Ed.*, 2019, **58**, 7526–7536.

19 X. Huang, K. Wang, Y. Wang, B. Wang, L. Zhang, F. Gao, Y. Zhao, W. Feng, S. Zhang and P. Liu, *Appl. Catal., B*, 2018, **227**, 322–329.

20 B. Dai, Y. Yu, Y. Chen, H. Huang, C. Lu, J. Kou, Y. Zhao and Z. Xu, *Adv. Funct. Mater.*, 2019, **29**, 1–9.

21 B. Dai, Y. Chen, S. M. Hao, H. Huang, J. Kou, C. Lu, Z. Lin and Z. Xu, *J. Phys. Chem. Lett.*, 2020, **11**, 7407–7416.

22 B. Dai, J. Fang, Y. Yu, M. Sun, H. Huang, C. Lu, J. Kou, Y. Zhao and Z. Xu, *Adv. Mater.*, 2020, **32**, 1–9.

23 R. Su, Y. Shen, L. Li, D. Zhang, G. Yang, C. Gao and Y. Yang, *Small*, 2015, **11**, 202–207.

24 L. Li, P. A. Salvador and G. S. Rohrer, *Nanoscale*, 2014, **6**, 24–42.

25 M. R. Morris, S. R. Pendlebury, J. Hong, S. Dunn and J. R. Durrant, *Adv. Mater.*, 2016, **28**, 7123–7128.

26 J. Malik, S. Kumar, P. Srivastava, M. Bag and T. K. Mandal, *Mater. Adv.*, 2021, **2**, 4832–4842.

27 H. T. Yi, T. Choi, S. G. Choi, Y. S. Oh and S. W. Cheong, *Adv. Mater.*, 2011, **23**, 3403–3407.

28 J. L. Giocondi and G. S. Rohrer, *J. Phys. Chem. B*, 2001, **105**, 8275–8277.

29 Y. Inoue, K. Sato and K. Sato, *J. Chem. Soc., Faraday Trans. 1*, 1989, **85**, 1765–1774.

30 J. Chen, H. Lu, H. J. Liu, Y. H. Chu, S. Dunn, K. Ostrikov, A. Gruverman and N. Valanoor, *Appl. Phys. Lett.*, 2013, **102**, 1–5.

31 H. G. Kim, D. W. Hwang and J. S. Lee, *J. Am. Chem. Soc.*, 2004, **126**, 8912–8913.

32 L. Wang, W. Wang, M. Shang, S. Sun, W. Yin, J. Ren and J. Zhou, *J. Mater. Chem.*, 2010, **20**, 8405–8410.

33 A. Kudo, K. Ueda, H. Kato and I. Mikami, *Catal. Lett.*, 1998, **53**, 229–230.

34 A. Kudo, K. Omori and H. Kato, *J. Am. Chem. Soc.*, 1999, **121**, 11459–11467.

35 W. Zhou, D. A. Jefferson and J. M. Thomas, *J. Solid State Chem.*, 1987, **70**, 129–136.

36 C. Chen, H. Ning, S. Lepadatu, M. Cain, H. Yan and M. J. Reece, *J. Mater. Chem. C*, 2015, **3**, 19–22.

37 I. M. Arabatzis, T. Stergiopoulos, M. C. Bernard, D. Labou, S. G. Neophytides and P. Falaras, *Appl. Catal., B*, 2003, **42**, 187–201.

38 V. Subramanian, E. Wolf and P. V. Kamat, *J. Phys. Chem. B*, 2001, **105**, 11439–11446.

39 C. G. Silva, R. Juárez, T. Marino, R. Molinari and H. García, *J. Am. Chem. Soc.*, 2011, **133**, 595–602.

40 J. Yang, D. Wang, H. Han and C. Li, *Acc. Chem. Res.*, 2013, **46**, 1900–1909.

41 J. S. Jang, D. J. Ham, N. Lakshminarasimhan, W. yong Choi and J. S. Lee, *Appl. Catal., A*, 2008, **346**, 149–154.

42 A. Y. Liu, R. M. Wentzcovitch and M. L. Cohen, *Phys. Rev. B*, 1988, **38**, 9483–9489.

43 R. B. Levy and M. Boudart, *Science*, 1973, **181**, 547–549.

44 Y. Wang, S. Song, V. Maragou, P. K. Shen and P. Tsiakaras, *Appl. Catal., B*, 2009, **89**, 223–228.

45 K. He, J. Xie, Z. Yang, R. Shen, Y. Fang, S. Ma, X. Chen and X. Li, *Catal. Sci. Technol.*, 2017, **7**, 1193–1202.

46 V. G. Pol, S. V. Pol and A. Gedanken, *Eur. J. Inorg. Chem.*, 2009, **2009**, 709–715.

47 S. Shanmugam, D. S. Jacob and A. Gedanken, *J. Phys. Chem. B*, 2005, **109**, 19056–19059.

48 F. H. Ribeiro, R. A. D. Betta, G. J. Guskey and M. Boudart, *Chem. Mater.*, 1991, **3**, 805–812.

49 Y. Oosawa, *J. Chem. Soc. Chem. Commun.*, 1982, **4**, 221–222.

50 M. J. Jacinto, P. K. Kiyohara, S. H. Masunaga, R. F. Jardim and L. M. Rossi, *Appl. Catal., A*, 2008, **338**, 52–57.

51 Z. Zhang, Y. Ma, X. Bu, Q. Wu, Z. Hang, Z. Dong and X. Wu, *Sci. Rep.*, 2018, **8**, 1–11.

52 A. T. Garcia-Esparza, D. Cha, Y. Ou, J. Kubota, K. Domen and K. Takanabe, *ChemSusChem*, 2013, **6**, 168–181.

53 H. G. Kim, T. T. Tran, W. Choi, T. S. You, P. S. Halasyamani and K. M. Ok, *Chem. Mater.*, 2016, **28**, 2424–2432.

54 M. K. Ehlert, J. E. Greedan and M. A. Subramanian, *J. Solid State Chem.*, 2016, **28**, 2424.

55 H. Yan, H. Zhang, M. J. Reece and X. Dong, *Appl. Phys. Lett.*, 2005, **87**, 1–4.

56 J. Wu, A. Mahajan, L. Riekehr, H. Zhang, B. Yang, N. Meng, Z. Zhang and H. Yan, *Nano Energy*, 2018, **50**, 723–732.

57 L. Jin, F. Li and S. Zhang, *J. Am. Ceram. Soc.*, 2014, **97**, 1–27.

58 H. G. Kim, J. S. Yoo and K. M. Ok, *J. Mater. Chem. C*, 2015, **3**, 5625–5630.

59 J. Tauc, R. Grigorovici and A. Vancu, *Phys. Status Solidi*, 1966, **15**, 627.

60 Y. Cui, J. Briscoe and S. Dunn, *Chem. Mater.*, 2013, **25**, 4215–4223.

61 Q. Fu, X. Wang, C. Li, Y. Sui, Y. Han, Z. Lv, B. Song and P. Xu, *RSC Adv.*, 2016, **6**, 108883–108887.

62 R. Li, F. Zhang, D. Wang, J. Yang, M. Li, J. Zhu, X. Zhou, H. Han and C. Li, *Nat. Commun.*, 2013, **4**, 1432–1437.

63 S. C. Abrahams, S. K. Kurtz and P. B. Jamieson, *Phys. Rev.*, 1968, **172**, 551–553.

64 G. Viola, K. Boon Chong, M. Eriksson, Z. Shen, J. Zeng, Q. Yin, Y. Kan, P. Wang, H. Ning, H. Zhang, M. E. Fitzpatrick, M. J. Reece and H. Yan, *Appl. Phys. Lett.*, 2013, **103**, 4.

65 Q. Jiang, H. Ning, Q. Zhang, M. Cain, M. J. Reece and H. Yan, *J. Mater. Chem. C*, 2013, **1**, 5628.

66 Z. Zhao, V. Buscaglia, M. Viviani, M. T. Buscaglia, L. Mitoseriu, A. Testino, M. Nygren, M. Johnsson and P. Nanni, *Phys. Rev. B: Condens. Matter Mater. Phys.*, 2004, **70**, 1–8.

67 Y. Wang, M. Zhang, J. Liu, H. Zhang, F. Li, C. W. Tseng, B. Yang, G. Smith, J. Zhai, Z. Zhang, S. Dunn and H. Yan, *Adv. Energy Mater.*, 2020, **10**, 6–11.

68 K. Page, J. Li, R. Savinelli, H. N. Szumila, J. Zhang, J. K. Stalick, T. Proffen, S. L. Scott and R. Seshadri, *Solid State Sci.*, 2008, **10**, 1499–1510.

69 B. Bondars, G. Heidemane, J. Grabis, K. Laschke, H. Boysen, J. Schneider and F. Frey, *J. Mater. Sci.*, 1995, **30**, 1621–1625.

70 A. Liibert and B. Leibold, *Sens. Actuators, B*, 1992, **8**, 253–256.

71 L. H. Bennett, J. R. Cuthill, A. J. Mcalister, N. E. Erickson and R. E. Watson, *Science*, 1974, **184**, 563–565.

72 I. Fujita, P. Edalati, Q. Wang, M. Watanabe, M. Arita, S. Munetoh, T. Ishihara and K. Edalati, *Scr. Mater.*, 2020, **187**, 366–370.

73 W. Huang, H. Meng, Y. Gao, J. Wang, C. Yang, D. Liu, J. Liu, C. Guo, B. Yang and W. Cao, *J. Mater. Chem. A*, 2019, **7**, 18538–18546.

74 M. Thangamuthu, C. Santschi and O. J. F. Martin, *Faraday Discuss.*, 2019, **214**, 339.

75 M. Wang, M. Ye, J. Iocozzia, C. Lin and Z. Lin, *Adv. Sci.*, 2016, **3**, 1600024.

76 S. Linic, P. Christopher and D. B. Ingram, *Nat. Mater.*, 2011, **10**, 911–921.

77 T. Zhang, W. Lei, P. Liu, J. A. Rodriguez, J. Yu, Y. Qi, G. Liu and M. Liu, *Chem. Sci.*, 2015, **6**, 4118.

78 J. Lan, X. Zhou, G. Liu, J. Yu, J. Zhang, L. Zhi and G. Nie, *Nanoscale*, 2011, **3**, 5161.

79 A. Phuruangrat, A. Maneechote, P. Dumrongrojthanath, N. Ekthammathat, S. Thongtem and T. Thongtem, *Mater. Lett.*, 2015, **159**, 289–292.

80 G. Yuan, G. Zhang, K. Li, F. Li, Y. Cao, J. He, Z. Huang, Q. Jia, S. Zhang and H. Zhang, *Nanomaterials*, 2020, **10**, 1–15.

81 J. D. Bobić, M. M. Vijatović, S. Greičius, J. Banys and B. D. Stojanović, *J. Alloys Compd.*, 2010, **499**, 221.

82 W. Qi, Y. Wang, J. Wu, Z. Hu, C. Jia, G. Viola, H. Zhang and H. Yan, *J. Am. Ceram. Soc.*, 2020, **103**, 28.

83 Y. Wang, M. Zhang, J. Wu, Z. Hu, H. Zhang and H. Yan, *J. Am. Ceram. Soc.*, 2021, **104**, 322–328.

84 W. Xiong, H. Porwal, H. Luo, V. Araullo-Peters, J. Feng, M. M. Titirici, M. J. Reece and J. Briscoe, *J. Mater. Chem. A*, 2020, **8**, 6564–6568.

85 K. Saito, K. Koga and A. Kudo, *Dalt. Trans.*, 2011, **40**, 3909.

86 C. Suryanarayana, *Prog. Mater. Sci.*, 2001, **46**, 1–184.

87 A. C. Larson and R. B. Von Dreele, GSAS Genralized Structure ANalysis System, *Los Alamos National Laboratory Report LAUR-86-748*, 1987.